Lung Digital Twin COVID-19 Infection: A Multiphysics - Multiscale HPC-Modeling Based on CFPD and Agent-Based Model Coupled Simulations

Alice **Novell**[a], Fernando **Muñoz**[b], Thaleia **Ntiniakou**[a], Arnau **Montagud**[a], Guillaume **Houzeaux**[a] and Ane Beatriz **Eguzkitza**[a,*]

[a]*Barcelona Supercomputing Center, 1-3 Plaça d'Eusebi Güell, 08034 Barcelona, Spain*

[b]*Universitat Politècnica de Catalunya, 1-3 Carrer de Jordi Girona, Les Corts, 08034 Barcelona, Spain*

ARTICLE INFO[†]

ABSTRACT

The present work is one of the three pieces (upper airways, lower conductive airways and respiratory zone) of a digital twin lung model developed by the *Physical and Numerical Modelling* research group from the CASE department in Barcelona Supercomputing Center (BSC). In particular, the study presents the solution of fluid flow and SARS-COV-2 particle transport in the lower conductive zone of the lungs, using a geometry based on patient specific images. The specific context of the current work is framed within the European Project: *CREXDATA: Critical Action Planning over Extreme-Scale Data*. Its general vision is to develop a generic platform for real-time critical situation management including flexible action planning and agile decision making over streaming data of extreme scale and complexity. One of the use cases of the project is the COVID-19 pandemic crisis, studying viral evolution in patients. To that end, the first step is to develop a mechanistic multiscale model to build a toolbox aimed at having a digital twin for the treatment of patients.

1. Introduction

In response to recent health crisis like the COVID-19 pandemic, researchers have utilized modeling to address complex challenges in crisis management. However, existing models often lack deep insights into viral evolution for novel therapeutic strategies [1, 2]. Our aim is to obtain a multiscale, multicellular, spatiotemporal model for simulating lung tissue infected by SARS-CoV-2, spanning from organ to cell level. This model aims to facilitate the discovery of patient-specific therapeutic targets and enable full-sized lung organ simulations.

Our approach integrates Alya [3] and PhysiBoSS [4] simulators for optimized, patient-specific interventions. Alya,

a HPC multiphysics tool, simulates airflow in the lung airways and viral particle transport, while PhysiBoSS, an agent-based tool, assesses alveolar states and cellular impacts.

This workflow can be summarized in:

1. The transport of viral particles in a mesh geometry of the lower conducting airways, considering up to 17th generation.
2. Coupling with the lung respiratory zone, to assess the viral deposition in the alveolar tissue.
3. Simulation of cell-level infection evolution in the epithelium.

In the current work, our focus lies on the first step of the proposed workflow: simulating airflow and viral aerosol transport in the lower conducting airways to evaluate the fraction of inhaled particles that reach the respiratory zone.

2. Methodology

This section describes the geometry and the computational mesh in Sec. 2.1, how the airflow simulations are conducted in Sec. 2.2, and the method for the particle transport in Sec. 2.3.

2.1. Geometry and mesh description

The geometry is patient-specific from generation 0 to 3 and synthetically generated from generation 3 to $\sim$ 17. The patient-specific part is reconstructed from a clinically
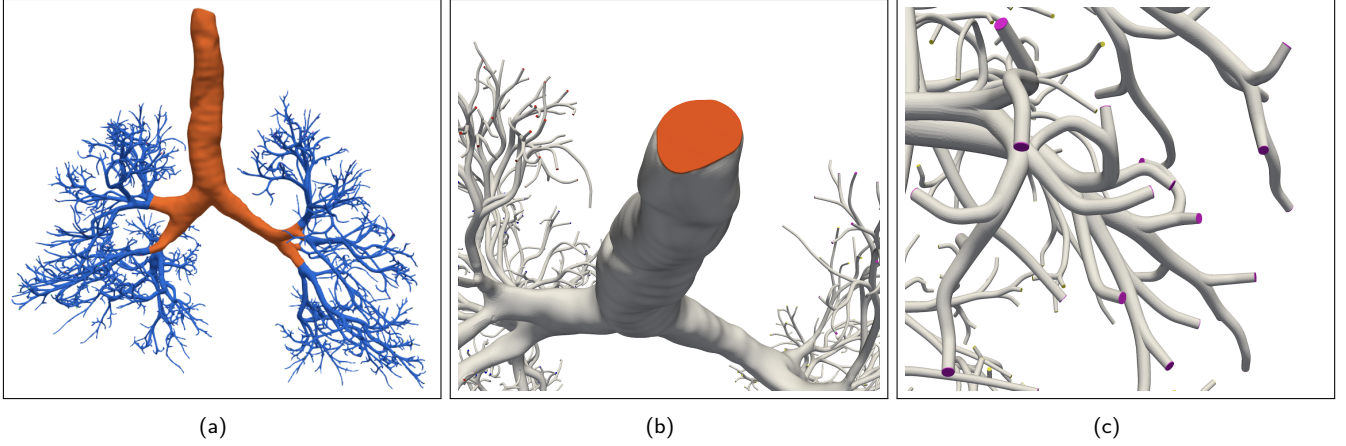
Figure 1: (a) Three dimensional geometry of airways, with patient-specific part shown in orange and synthetic part shown blue. (b) Trachea inlet. (c) Terminal outlets.

	Very shallow	Shallow	Normal	Deep	Very deep
$Q_{\max}$ (L/min)	7.5	15	22.5	30	60
$V_{inhaled}$ (L)	0.159	0.318	0.477	0.637	1.274

Table 1

Characteristics of 5 breathing patterns in a sinusoidal model.

acquired computed tomography (CT) scan, and each terminal is connected to the corresponding synthetically generated extension to obtain the conducting zone of the airways (Fig. 1). The synthetic airways are computed following [5]. An initial study to asses the fidelity of the resulting geometry with anatomical experimental data found in literature is performed.

An unstructured mesh is employed, due to the complex shape of the geometry. The mesh has more than 45M elements and is hybrid, made of tetrahedrons with prism layers at the wall to resolve the wall boundary layer profile.

2.2. Airflow simulations

In order to obtain the airflow simulations, we solve the Navier-Stokes equations. The numerical model to solve these equations is based on a stabilized finite element method. A description of this numerical method can be found in [6].

Regarding boundary conditions, an initial approach involves imposing flow rate at the trachea inlet and setting zero pressure at all outlets, aligning with existing literature for result validation [7, 8]. However, further exploration of alternative boundary conditions is undertaken to obtain a

more accurate solution that better captures the underlying physical phenomena.

We simulate both stationary flows and sinusoidal breathing patterns. The parameters are shown in Tab. 1. In the case of stationary flow, a constant flow rate of $Q_{\max}$ is imposed at the trachea, while for dynamic breathing a sinusoidal function is imposed:

$$
\begin{aligned}
Q_{\text{trachea}}(t) = \frac{d\Delta V}{dT} &= \left(\frac{V_{\text{inh}}\,\pi}{T}\right) \sin\left(\frac{2\pi}{T}t\right) \\
&= Q_{\max} \sin\left(\frac{2\pi}{T}t\right), \quad (1)
\end{aligned}
$$

where the breathing cycle period T is 4 seconds in all cases.

2.3. Particle transport

The transport of particles is simulated in a Lagrangian frame of reference, following each particle individually. From the numerical point of view, the main assumptions to develop the model are: particles are assumed sufficiently small to neglect their effect on the air, therefore, a one way coupling is considered; particles do not interact with each other; and particle rotation is neglected.

Particles are injected at the trachea inlet following a uniform distribution. For the steady simulations, all particles are released at the initial time step. For the unsteady simulations, a number of particles proportional to the flow rate are injected at each timestep during inspiration. Different particle sizes in a range around 120 nm are considered, representing viral particles [9].

3. Results

This section presents the results of the study. In more detail, Sec. 3.1 presents and analysis of the conductive zone
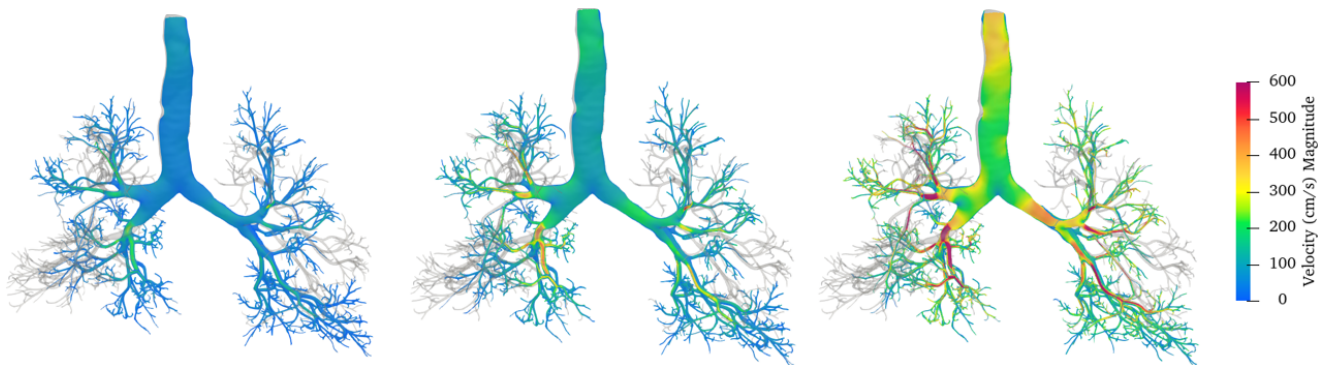
(a) Velocity streamlines in the bifurcating model for different airflow rates: (left) 7.5 L/min, (middle) 15 L/min, and (right) 30 L/min.
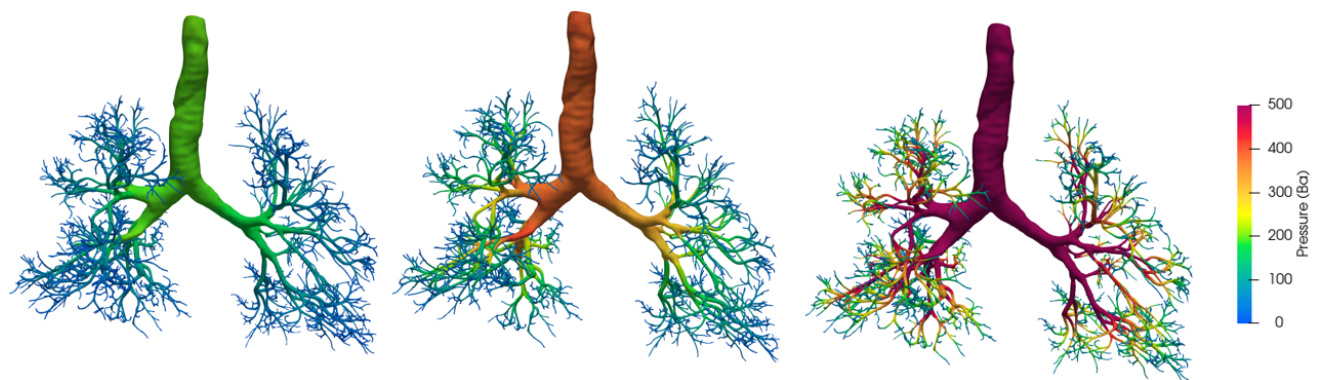
(b) Pressure for three different airflow rates: (left) 7.5 L/min, (middle) 15 L/min, and (right) 30 L/min.

Figure 2: Visualization of the velocity streamlines and the pressure distribution in the lung model.
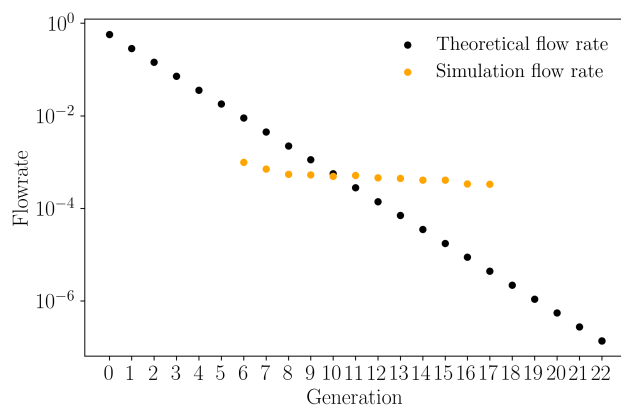

**Figure 3:** Flow rate per generation for 30 L/min.

geometry, Sec. 3.2 investigates stationary simulations of the conductive zone, and Sec. 3.3 looks at transient simulations.

3.1. Analysis of the conductive zone geometry

The validation of the conductive zone geometry confirms the model's adherence to anatomical structures, while highlighting some differences. The relationship between airway diameter and generation shows close agreement with experimental data in the patient-specific portion (generations 0–2), whereas the synthetic geometry exhibits a faster diameter reduction.

Characterization of branching indicates a deviation from ideal dichotomous branching, as not all branches divide beyond generation 8, resulting in a distribution of terminal branches centered around generation 11. Moreover, the terminal diameters remain fixed regardless of generation, leading to abrupt changes in diameter at higher generations.

The model's lobe-specific terminal distribution is anatomically realistic, with the right side containing more terminals and the right middle lobe having the fewest. However, the observations that not all branches reach the same generation, combined with inaccuracies in diameters, underscore the need for improving the geometry and setting boundary conditions that accurately capture the resulting pressure differences.
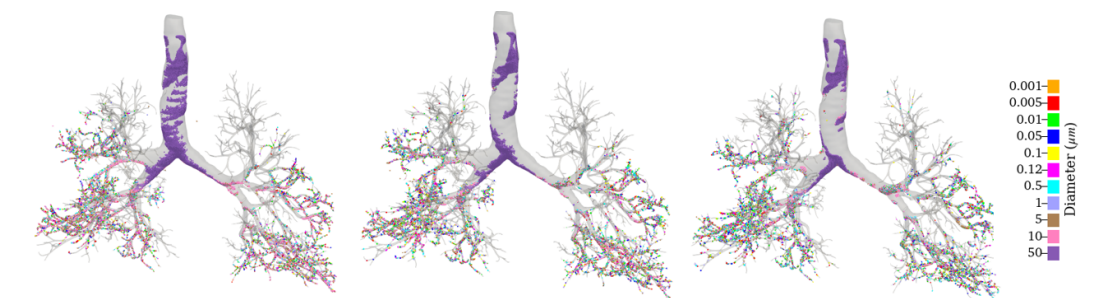
(a) Particle deposition for three different airflow rates: (left) 7.5 L/min, (middle) 15 L/min, and (right) 30 L/min.

(b) SARS-CoV-2 particle deposition for three different airflow rates: (left) 7.5 L/min, (middle) 15 L/min, and (right) 30 L/min.

Figure 4: Visualization of the particle deposition in the lung model.

3.2. Stationary simulations of the conductive zone

The stationary simulations of the conductive zone are validated to ensure solution accuracy and stability. Velocity profiles at various positions in the airways are validated against prior studies, revealing similar velocity trends. Reynolds number calculations confirm laminar or transitional flow, justifying the neglect of turbulence.

The air velocity streamlines shown in Fig. 2a reveal peak velocities after the initial bifurcation areas of all five main lobes, marking the transition from the patient-specific to the synthetic model. This peaks in velocity are likely due to the abrupt changes in diameter at these transition points.

Flow rate comparisons with theoretical values as depicted in Fig. 3 highlight discrepancies due to uniform terminal diameters and boundary conditions, which fail to account for realistic variability across generations.

The pressure distribution results, see Fig. 2b, show a steady decrease from the trachea to lower generations, with maximum pressure observed near the tracheal walls, as expected. Higher flow rates exhibit more significant pressure drops in lower airways.

Particle deposition patterns as found in Fig. 4a reveal that larger particles, e.g., 50 μm, predominantly deposit in the trachea, with deposition spreading into deeper airways as particle size decreases. The SARS-CoV-2 particle deposition, see Fig. 4b, shows higher concentrations in the bronchial regions for higher flow rates.

Flow and particle outflow analyses demonstrate a consistent pattern of higher outflow in the right lung, with the right middle lobe showing the lowest outflow. Particle outflow is inversely related to flow rate, with higher deposition observed at increased flow rates. Larger particles exhibit greater deposition than smaller particles, emphasizing size-dependent behavior in particle transport and deposition.

3.3. Transient Simulations: Breathing cycle

SARS-CoV-2 particle transport is visualized at the start of inhalation ($t = 0.1, 0.2, 0.3s$) and exhalation ($t = 2.1, 2.3, 2.5s$) in Fig. 5.

Deposition progresses as particles initially deposit in the deep airways during inhalation and then in the first generations during exhalation, see Fig. 6.

The percentage of particles exiting through the terminal airways in each lobe as depicted in Fig. 7a show that more particles exit through the right lung than the left, with the lowest outflow observed in the right middle lobe.

The percentage distribution of deposited, outgoing, and exhaled particles for each flow rate, see Fig. 7b, shows high deposition percentages, particularly for 60 L/min and 15 L/min. It is noted that deposition may be overestimated due
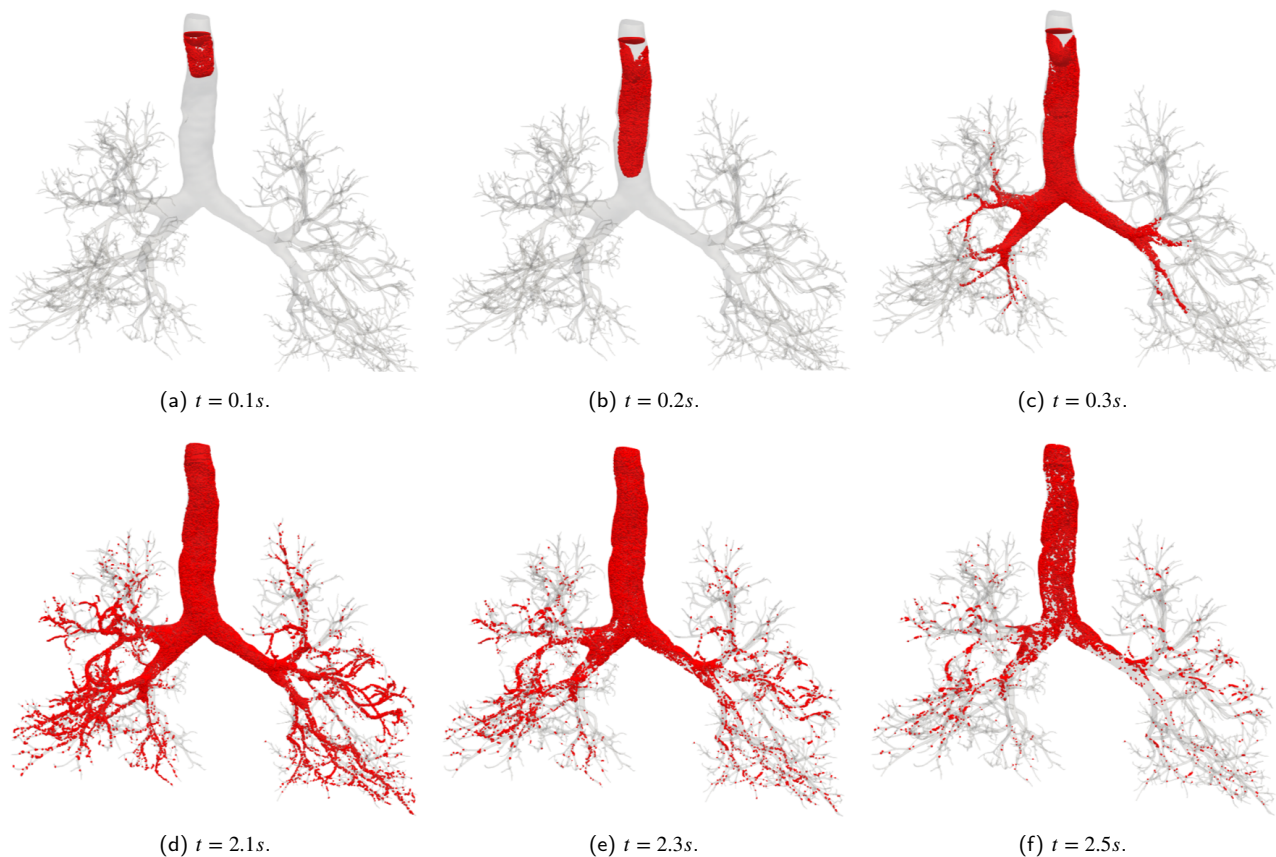
(a) $t = 0.1s$.   (b) $t = 0.2s$.   (c) $t = 0.3s$.

(d) $t = 2.1s$.   (e) $t = 2.3s$.   (f) $t = 2.5s$.

Figure 5: Particle transport at different time stances for 30L/min.

to the assumption that all particles touching the wall remain deposited, while in reality, not all particles stay attached.

4. Conclusions

This study examines SARS-CoV-2 particle behavior within the conductive zone of the respiratory system, providing key insights into particle deposition dynamics. The results demonstrate that airflow rates significantly affect deposition patterns, with elevated airflow (such as during physical exertion) increasing the likelihood of particles reaching deeper regions. This suggests a heightened risk of infection in the lower respiratory tract under certain conditions.

However, the current model has limitations. The synthetic geometry used diverges from anatomical accuracy, with inconsistencies in branch diameters and incomplete branching to terminal generations.

5. Future work

Future efforts will focus on addressing the geometric limitations of the conductive zone model by incorporating anatomically accurate branching structures and implementing more sophisticated boundary conditions, such as assigning unique conditions to individual outlets to better simulate physiological variations.

Moreover, expanding the model to include a comprehensive respiratory zone geometry, currently under development, will enable a more detailed analysis of particle behavior throughout the entire respiratory tract.

Additionally, improvements to the particle deposition model will account for particle bouncing upon wall contact, offering a more accurate representation of deposition dynamics. The model will also be adapted to study the impact of pathological conditions, such as asthma and COPD, by modifying airway geometries to reflect disease-specific changes.

Coupling the model with PhysiBoSS will enable detailed simulations of virus-cell interactions, which will provide deeper insights into viral behavior and infection progression.
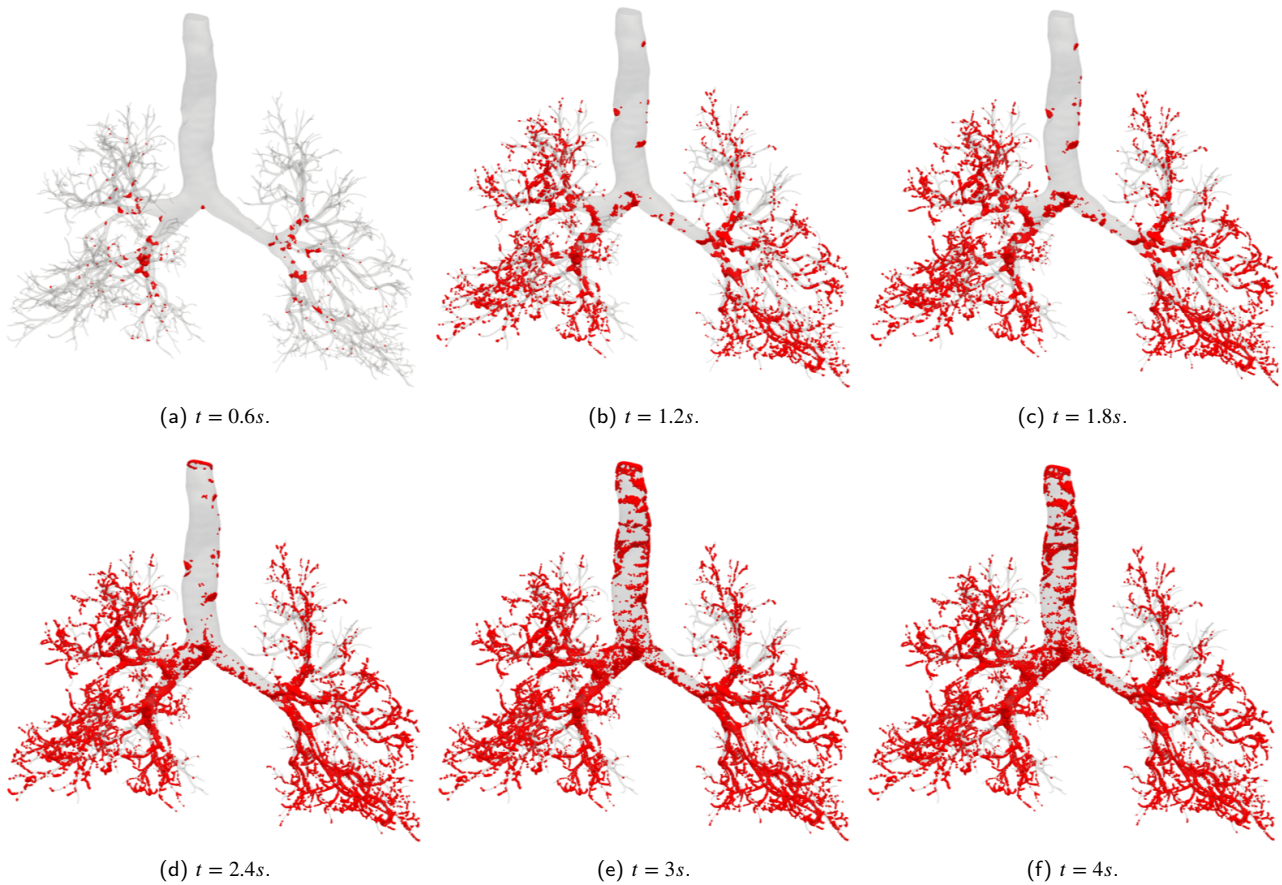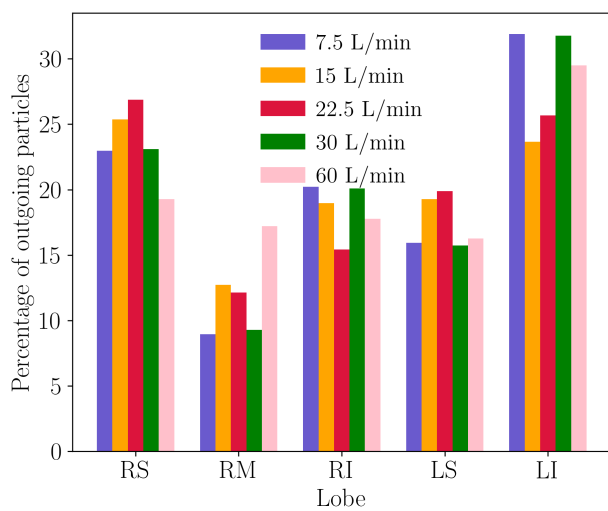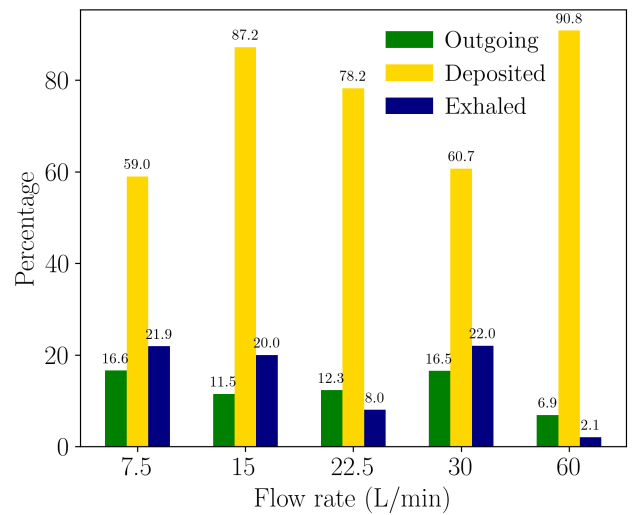
(a) $t = 0.6s$.

(b) $t = 1.2s$.

(c) $t = 1.8s$.

(d) $t = 2.4s$.

(e) $t = 3s$.

(f) $t = 4s$.

Figure 6: Deposition progression at different time instances for 30L/min.

(a) Percentage of outgoing particles through the terminals in each lobe for the five flow rates.

(b) Percentage distribution of deposited, outgoing, and exhaled particles for the five flow rates.

Figure 7: Distributions of particles.

References

[1] I. Cooper, A. Mondal, C. G. Antonopoulos, A SIR model assumption for the spread of COVID-19 in different communities, Chaos, Solitons & Fractals 139 (2020) 110057. doi:10.1016/j.chaos.2020.110057.

[2] J. Shang, G. Ye, K. Shi, Y. Wan, C. Luo, H. Aihara, Q. Geng, A. Auerbach, F. Li, Structural basis of receptor recognition by SARS-CoV-2, Nature 581 (2020) 221–224. doi:10.1038/s41586-020-2179-y.

[3] M. Vázquez, G. Houzeaux, S. Koric, A. Artigues, J. Aguado-Sierra, R. Arís, D. Mira, H. Calmet, F. Cucchietti, H. Owen, A. Taha, E. D. Burness, J. M. Cela, M. Valero, Alya: Multiphysics engineering simulation toward exascale, Journal of Computational Science 14 (2016) 15–27. doi:10.1016/j.jocs.2015.12.007.

[4] M. Ponce-de Leon, A. Montagud, V. Noël, A. Meert, G. Pradas, E. Barillot, L. Calzone, A. Valencia, PhysiBoSS 2.0: a sustainable integration of stochastic Boolean and agent-based modelling frameworks, npj Systems Biology and Applications 9 (1) (2023) 54. doi:10.1038/s41540-023-00314-4.

[5] M. H. Tawhai, P. Hunter, J. Tschirren, J. Reinhardt, G. McLennan, E. A. Hoffman, CT-based geometry analysis and finite element models of the human and ovine bronchial tree, Journal of Applied Physiology 97 (2004) 2310–2321. doi:10.1152/japplphysiol.00520.2004.

[6] G. Houzeaux, R. Aubry, M. Vázquez, Extension of fractional step techniques for incompressible flows: The preconditioned Orthomin(1) for the pressure Schur complement, Computers and Fluids 44 (2011) 297–313. doi:10.1016/j.compfluid.2011.01.017.

[7] M. S. Islam, P. Larpruenrudee, A. R. Paul, G. Paul, T. Gemci, Y. Gu, S. C. Saha, SARS CoV-2 aerosol: How far it can travel to the lower airways?, Physics of Fluids 33 (6 2021). doi:10.1063/5.0053351.

[8] T. Gemci, V. Ponyavin, Y. Chen, H. Chen, R. Collins, Computational model of airflow in upper 17 generations of human respiratory tract, Journal of Biomechanics 41 (2008) 2047–2054. doi:10.1016/j.jbiomech.2007.12.019.

[9] N. Zhu, D. Zhang, W. Wang, X. Li, B. Yang, J. Song, X. Zhao, B. Huang, W. Shi, R. Lu, P. Niu, F. Zhan, X. Ma, D. Wang, W. Xu, G. Wu, G. F. Gao, W. Tan, A Novel Coronavirus from Patients with Pneumonia in China, 2019, New England Journal of Medicine 382 (8) (2020) 727–733. doi:10.1056/NEJMoa2001017.